

Full length article

The role of emerging grain boundary at iron surface, temperature and hydrogen on metal dusting initiation



El Tayeb Bentria^a, Gawonou K. N'tsouaglo^a, Charlotte S. Becquart^b, Othmane Bouhali^c, Normand Mousseau^d, Fedwa El-Mellouhi^{a,*}

^a Qatar Environment and Energy Research Institute, Hamad Bin Khalifa University, P.O. Box 5825, Doha, Qatar

^b Univ. Lille, CNRS, INRA, ENSCL, UMR 8207, UMET, Unité Matériaux et Transformations, F 59000 Lille, France

^c Texas A&M University at Qatar, P.O. Box 23874, Doha, Qatar

^d Département de physique, Université de Montréal, Case postale 6128, succursale centre-ville, Montréal, QC H3C 3J7, Canada

ARTICLE INFO

Article history:

Received 2 February 2017

Received in revised form

10 June 2017

Accepted 23 June 2017

Available online 23 June 2017

Keywords:

Grain boundaries

Metal dusting

CO dissociation

DFT

Molecular dynamics

ABSTRACT

We conduct a multiscale modeling of different iron systems exposed to carbon-rich atmospheres by means of density functional theory and reactive molecular dynamics in order to evaluate the effects of temperature, gas content and surface defects such as emerging grain boundaries and grooves on CO dissociation rate. Comparative density functional theory calculations of carbon adsorption energies on clean surface and the groove area show that grooves have preferential binding sites, explaining why emerging grain boundaries are more severely attacked by metal dusting corrosion. Molecular dynamical simulations using a ReaxFF potential on iron $\Sigma 3$ and $\Sigma 5$ emerging grain boundaries on (111) and (210) surfaces, respectively, also demonstrate the enhanced CO dissociation rate within the grooves area. Analysis of CO dissociation and recombination events on these systems demonstrates quantitatively the dual role of hydrogen as a CO dissociation enhancer and reactant with dissociated carbon atoms. By carefully characterizing reaction mechanisms as a function of reactant content, we provide a linear correspondence between CO dissociation variation as function of temperature and the experimental measurement of metal dusting corrosion rate.

© 2017 Acta Materialia Inc. Published by Elsevier Ltd. All rights reserved.

1. Introduction

Surfaces and interfaces and their orientations in crystalline structures play a crucial role in the adsorption and dissociation of molecules acting as preferential sites for corrosion and crack initiation [1]. Despite significant advances achieved in the preparation of high-quality metallic surfaces, surface defects such as vacancies, dislocations and emerging grain boundaries on the surface are inevitable. These defects affect the homogeneity of the surface by enhancing its catalytic activity and favoring the adsorption and segregation of impurities and molecules that might trigger corrosion. For example, metal dusting, a destructive type of corrosion, takes place when materials are exposed to high-carbon containing atmospheres namely hydrocarbons, such as CH_4 and CO at high temperatures, typically between 600 K and 1100 K [2], leading to the breakdown of bulk metals into metal powders.

This process is caused by hydrocarbons that dissociate readily on the metal surface followed by carbon atom diffusion into the subsurface to form cementite. At more advanced stages, carbon diffusion in the bulk is observed leading to cementite precipitate formation, while metal diffusion from bulk to the surface is observed thus increasing the reactivity of the surface. Beyond dusting, the kinetics of hydrocarbon dissociation and diffusion in iron through surfaces or grain boundaries plays a general role in steel corrosion and steelmaking processes [3].

Although carbon adsorption, segregation and diffusion in Fe surface and grain boundaries have been thoroughly studied experimentally and theoretically [2,4–7], some of the factors affecting the CO dissociation rate, such as defective surfaces with emerging GBs, temperature and hydrogen that could affect the metal dusting phenomenon are still not fully understood. Hydrogen effect on iron surfaces attracted a good deal of attention, both in DFT studies dealing with its adsorption, absorption, dissolution, and diffusion energetics on iron bulk and surfaces [10–12] as well as using reactive molecular dynamics simulations [13] to

* Corresponding author.

E-mail address: felmellouhi@hbku.edu.qa (F. El-Mellouhi).

elucidate the mechanisms of hydrogen interaction with pure and defective iron using ReaxFF potentials. However, very few studies have focused on the effect of emerging GBs from the atomic modeling point of view. Among those, Ho-Seok et al. [8] demonstrated by means of molecular dynamics (MD) simulation using the Embedded Atom Model (EAM) potential how Ga could penetrate Al bicrystal along the $\Sigma 5$ symmetric tilt boundary emerging at the surface. Ga penetration seems to constitute the early stages of liquid metal embrittlement. MD simulations show that penetration of liquid Ga through certain types of grain boundaries marks a significant enhancement upon applying stress [8]. Frolov et al. [9] studied, also by means of EAM potentials, the effect of emerging $\Sigma 5$ GB on Cu causing structural transformations at interfaces. Reversible first order transformations between phases were observed by varying temperature or injecting point defects in the boundary region. Furthermore, experimental observation of emerging GB on metal dusting by Chun et al. [2] demonstrated that the localized corrosion of iron profuse primarily via the grain boundary regions.

The main goal of the present study is to further expand our understanding of the early stages of metal dusting corrosion by means of atomistic simulations. We employ a multiscale computational methodology to study the adsorption and segregation of carbon atoms on $\Sigma 3$ and $\Sigma 5$ GBs emerging at a free surface (FS) of pure BCC-Fe. Density Functional Theory calculations (DFT) provide accurate quantitative results about adsorption, site preference and segregation energies. Nevertheless, the high computational cost associated with surface calculations limits the number of atoms considered to a few hundred atoms. Because we are dealing with extended defects on surfaces that propagate to the bulk region as well, physically-relevant models require thousands of atoms, making the standard DFT calculation prohibitively expensive. To access the right model size, we make use of empirical molecular dynamics that can handle larger numbers of atoms at the cost of interatomic potential accuracy. To limit the impact of the potential, we select a recent version of the reactive force field (ReaxFF) potential (2016) [13] originally derived by Van Duin et al. in (2011) [14] and fitted to various DFT and experimental data. This potential reproduces the catalytic activities of C, O, H on BCC-Fe surface and has proved to be efficient in simulating the adsorption and dissociation phenomena with good accuracy [15]. We used this potential to investigate CO dissociation on a BCC-Fe surface as a function of temperature, the effect of hydrogen molecules, and additional factors influencing the CO dissociation rates, including defective surface properties such as a GB emerging at the surface, quantities that have been poorly explored to date.

To this end, a defective region at the meeting point between the GB and the FS with missing Fe atoms is created to simulate a groove. A groove may emerge from a local nanoscale damage or nano-indentation and act as a corrosion initiation site. We explore the role of the groove in accelerating the C adsorption and trapping as well as the CO dissociation rate once the surface is exposed to a mixture of CO and H₂ gases by following the dynamics of their deposition. We derive a relationship between CO dissociation rate and the variation of temperature, thus elucidating its impact on the metal dusting corrosion rate. We also analyze how hydrogen enhances the CO dissociation rate on Fe surfaces and finally confirm the effect of grooves as a CO dissociation rate enhancer.

2. Computational methods

2.1. Density functional theory calculation

DFT calculations are carried out using the GGA-PBE exchange-correlation functional with the projector augmented wave (PAW)

method [16], implemented in the Vienna Ab initio simulation package (VASP) [17,18]. Spin-polarized treatment is used in all calculations with $2 \times 5 \times 1$ k-point sampling. Total energies are calculated with a kinetic energy cutoff of 400 eV for all models. Convergence criteria of 0.1 meV/atom and 10^{-3} Å are used for total energy and structure relaxation respectively.

The model consists of a BCC-Fe slab of 158 atoms with a $\Sigma 3$ GB emerging at the (111) surface enclosed in a periodic simulation box of $14.89 \times 8.10 \times 28.07$ Å³. To guarantee negligible interaction between surfaces due to periodic boundary conditions, the size of the vacuum region is set to 8 Å (see Fig. 1). Two of the overall ten atomic layers at bottom of the slab are fixed to simulate infinite bulk. In a previous report [19], we demonstrated that, for CO molecules adsorbed on a BCC-Fe surface, finite size effects lead to a significant slow convergence of the adsorption energy as a function of the simulation box size affecting the molecules' dissociation barrier as well. One of the major contributors to this slow convergence is the self-interaction due to the dipole moment of the CO molecule. In order to minimize this contribution while keeping the size of the simulation box tractable for DFT calculations, adsorption energies are restricted to one carbon atom only at different positions within the $\Sigma 3$ GB emerging at the (111) surface. In the case of one carbon atom, the adsorption energy is the energy difference between the surface with adsorbed atoms and the clean surface and isolated carbon atoms: $E_{ad} = E_{Fe-ad} - E_{Fe} - E_{C-iso}$

2.2. Models for CO, H₂ adsorption on Fe surfaces

Empirical molecular dynamics calculations are performed on two grain boundaries: $\Sigma 3$ and $\Sigma 5$, emerging at the (111) and (210) surfaces of BCC-Fe, respectively. For that purpose, two matching slab models are built together with their corresponding ideal slabs to ensure equal footing setups (comparable adsorption surface area). The $\Sigma 3$ ($\Sigma 5$) GB emerging at the surface model consists of 4100 (4500) atoms enclosed in a simulation box of $61.8 \times 72.7 \times 19.8$ Å³ ($22.8 \times 61.1 \times 65.9$ Å³), leading to surface areas of 14.5 nm² for $\Sigma 3$ and 20.5 nm² for $\Sigma 5$ GB. The corresponding clean surface model has to have an equal surface area, we thus build a 4788 (5400) atom slab, within a periodic simulation box of $59.4 \times 20.2 \times 70.7$ Å³ ($28.5 \times 61.0 \times 70.0$ Å³) i.e. around 15 (22) layers, leading to a free adsorption surface area of 14.4 nm² (111) and (210 nm²) for (210) surfaces. For both GB models, we include the groove area of about $4.0 \times 8.1 \times 5.5$ Å³ in calculating the total surface (see Fig. 2).

Molecular dynamics simulations are performed using the Large-scale Atomic/Molecular Massively Parallel Simulator (LAMMPS) code [20]. The equations of motion are integrated using the

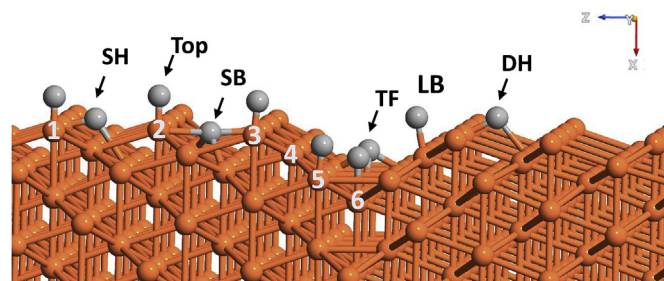


Fig. 1. Model of Fe $\Sigma 3$ symmetrical tilt grain boundary emerging at the (111) surface. Iron atom sites used in carbon adsorption are labeled from 1 to 6. LB corresponds to the Long Bridge adsorption site, SB to the Short Bridge, TF to the Three Fold, SH to the Shallow Hollow, and DH to the Deep Hollow. TF 5–6 corresponds to the three fold position between Fe atom 5 and 6. The groove is clearly visible by the V-shape at the center of the sample.

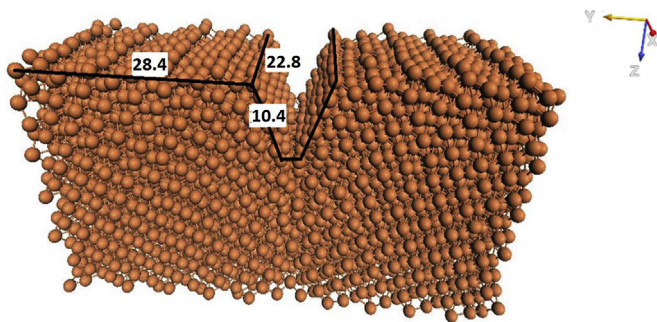


Fig. 2. Relaxed $\Sigma 5$ grain boundary emerging at the (210) surface with a nano-indentation or a groove area (MD simulation with 4500 atoms). The dimensions of the surface and the groove are indicated in angstroms.

velocity-Verlet method in the canonical ensemble (NVT) under a constant number of atoms, volume and temperature. In general, time step for empirical MD should be 1 order of magnitude smaller than the shortest motion or approximately 0.5–1.0 fs. Using the ReaxFF interatomic potential requires the use of an even smaller time step; to ensure the correct dynamics with atomic charge and bond order fluctuations, a time step of 0.2 fs is selected. Simulations are run for up to 400 ps; during the equilibration stage, temperature is raised gradually by 0.01 K per MD step.

We use the “deposit” command of the LAMMPS package to insert the molecules into the vacuum region. This feature, which simulates better the gas flow, allows us to insert molecules randomly in space every 125 time steps. Molecules are inserted gradually in the box starting at least 0.5 nm away from the surface and its periodic counterpart to avoid inserting particles close to the surface. A “fix wall” command is used to prevent the possibility of a particle escaping out of the vacuum region. It is worth mentioning that initiating the calculation with a large number of deposited CO and H₂ molecules would prevent the observation of CO reacting with the BCC-Fe surface in favor of the formation of complexes in the vacuum region. All models have thick vacuum region of 30 Å to ensure that we avoid any significant raise in the pressure upon the molecular insertion. This large vacuum also enables us to insert a sufficient amount of a 50%CO:50%H₂ gas mixture reacting with (111) and (210) iron surfaces until they become fully covered or in other words until the surface coverage saturation is reached.

The systems that we have studied are composed of flexible molecules with flexible bonds that exhibit translational, rotational, torsional, and vibrational motion, hence the ReaxFF represents a convenient way to compute the interatomic interaction. ReaxFF is a general bond-order-dependent force field that provides accurate descriptions of bond breaking and bond formation (e.g., [13,21]). The main difference with traditional unreactive force fields is that in ReaxFF the connectivity is determined by bond orders calculated for interatomic distances that are updated every MD step. This allows for the adaption of each atom force field as a function of its coordination. In order to account for non-bonded interactions such as van der Waals and Coulomb interactions in a system with changing connectivity, these interactions are calculated between every pair of atoms, irrespective of connectivity, and all excessive close-range nonbonded interactions are avoided by the inclusion of a shielding term [21]. In addition, ReaxFF accounts for polarization effects by using a geometry-dependent charge calculation scheme. A full description of ReaxFF potential functions can be found in Ref. [22].

The dissociation rate in this work is calculated using a simple script that reads MD dumping files at required time steps and calculates the distance between C and O atoms. If it exceeds 1.7 Å,

the CO molecule is considered to be completely dissociated [6].

3. Results and discussion

3.1. Density functional theory results

The adsorption energy of carbon atoms on the $\Sigma 3$ symmetrical tilt grain boundary emerging at the bcc-Fe (111) surface is calculated for 13 different adsorption sites. Fig. 1 presents a schematic presentation of the $\Sigma 3$ emerging at the (111) surface, with iron asymmetric adsorption sites numbered from 1 to 6, along with the different types of carbon adsorption which are: LB -Long Bridge, SB -Short Bridge, TF-Three Fold, SH -Shallow Hollow, and DH -Deep Hollow. TF 4–5 for example represents the Three Fold position between iron atom number 4 and 5, S-DH presents the Deep Hollow position on the Surface (near site 1). As indicated above, due to the limited size of the simulation box that could be treated using DFT accuracy, we restrict the study to the $\Sigma 3$ grain boundary since this system can be correctly modeled using a few hundred atoms. Furthermore, we calculate the adsorption of a single carbon atom rather than that of a CO. This approach minimizes the finite size effects and allow us to better capture the impact of the surface defect, i.e. the groove, on the C adsorption energies, and its potential to act as a preferential adsorption (trapping) site. Fig. 3 reports the calculated carbon adsorption energies at the stable adsorption sites. For each configuration, we perform full structural relaxations of the C atom as well as its 12 to 20 nearby neighboring Fe atoms while fixing all remaining atoms. During structural relaxation, some initial adsorption sites turn out to be unstable, causing the C atoms to move to more stable sites. This is the case, for instance, for the Top 5 configuration that relaxes to the TF 4–5 site, explaining why this site is not reported in Fig. 3. We first compare the C adsorption energies for the clean (111) surface, away from the groove area. These positions are the Top 1, Top 2, shallow-hollow (SH), and deep-hollow (DH) positions (they are shown in green). The remaining 9 adsorption sites cover the possibilities in the groove area (they are shown in blue). As can be seen from Fig. 3, the adsorption energies on the surface in the region far from groove are close to the ones we calculated for the clean non defective surface and to those of Huo *et al* [11], although they are slightly lower. This shows that strain effects associated with the emerging GB propagate outside the groove, leading to preferred adsorption sites in its vicinity as compared with the perfect surface. Interestingly, the Top positions on the defective surface become gradually more and more stable as they are closer to the groove (sites 1 → 6), indicating a trapping effect: adsorption energies evolve from –5.6 eV at the Top 1 site to –7.64 eV at the bottom of the groove (Top 6). Further analysis reveals that this considerable energy variation as a function of the Top position is due to the morphology of the surface. For example, Top 6 position inside the groove allows the carbon atom to make more bonds with the nearest Fe atoms due to the slant morphology.

With respect to other positions, we find that carbon atoms prefer TF adsorption positions both in non-defective FS and GB groove while the Top positions are likely to be visited during the carbon diffusion on the surface. Our calculations show that TF energies in the groove area are 0.9 eV lower than the most stable site in the clean surface. In addition, the groove area counts additional TF positions (represented by blue triangles in Fig. 3) compared to the clean surface and perfect $\Sigma 3$ tilt GB, which might lead to a larger C deposition and adsorption rate within the groove area.

The preferential groove area adsorption sites can be interpreted by looking at the electronic density distribution at the surface and a topological bonding analysis. We present in Fig. 4 the electronic charge density for the $\Sigma 3$ GB emerging at the (111) surface at

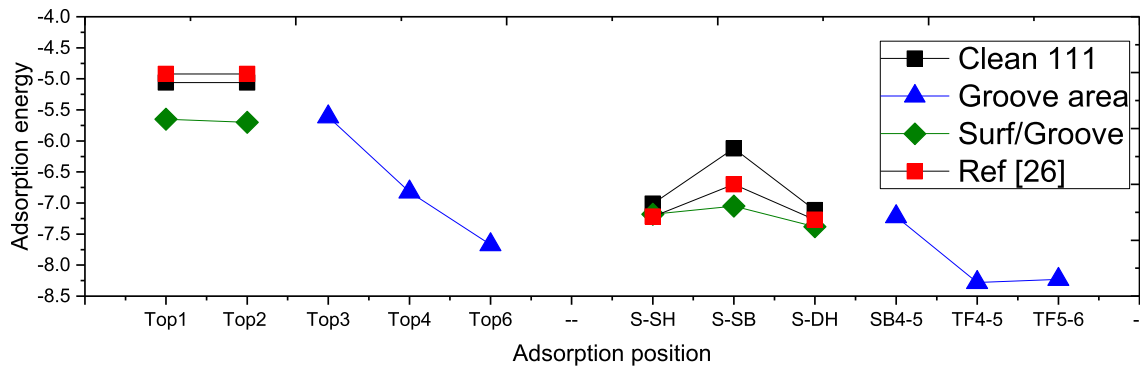


Fig. 3. Adsorption energies (in eV), for a carbon atom on a $\Sigma 3$ GB emerging on the (111) free surface. The positions are labeled (Top), Deep Hollow (DH) and Shallow Hollow (SH). The adsorption site number 1 is the furthest from the groove, and adsorption site number 6 is the closest to the groove (see Fig. 1). The black squares refer to the adsorption energy on a free, non-defective (111) surface; results from Ref. [19] are plotted in red squares for comparison. Adsorption energies far from the groove surface are represented in green, while those within the groove area are presented by blue triangles. (For interpretation of the references to colour in this figure legend, the reader is referred to the web version of this article.)

electron density iso-values of $1.43 \text{ e}/\text{\AA}^3$. The charge transfer from the surface to the adsorbed carbon atom at site Top 2 is visible in the figure explaining the relatively high adsorption/segregation energies. The electronic charge density is equally distributed on the surface indicating that despite the variation in the structural morphology of the surface, the metallic bond character of BCC-Fe imposes a uniform electronic density across the entire surface. Hence one may conclude that the preferential groove area adsorption sites reported in the previous paragraph has other origins than the electronic distribution.

The preferential C adsorption in the groove area can be rather fully understood from topological analysis of the bond formations: it is well known that in the early stages of metal dusting, carbon and iron form cementite Fe_3C near the surface characterized by 6 Fe–C bonds of around 2.0 \AA with a total of 4 participating electrons. A comparable coordination can be formed only if the interstitial C atoms is located in bulk BCC-Fe interstitial octahedral sites which is smaller than Fe_3C octahedral site and thus encourages carbon segregation to the surface and planar defects [23]. This renders the formation of cementite in pure bulk more difficult starting from the perfect pure surface than from a defective one. On the other hand, assuming that vacancies are present, the substitutional site in the bulk introduces a large vacuum space in which C can make 3 bonds only with its Fe nearest neighbors, which is not favorable as well. Interestingly, the groove region offers the suitable topological environment to form a four-fold C–Fe bonding since it offers slightly larger atomic distances than the ideal bulk structure, hence giving rise to the very first Fe_3C nucleation seeds.

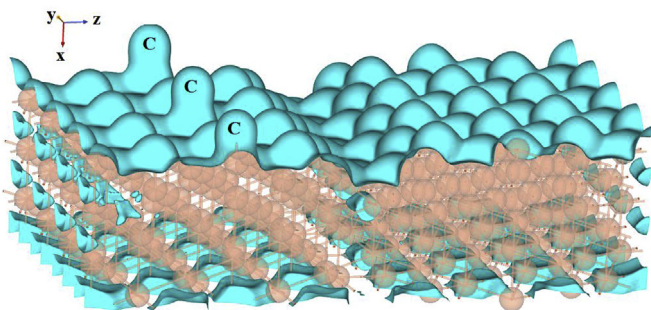


Fig. 4. Electron charge density at an isovalue of $1.43 \text{ e}/\text{\AA}^3$ for a $\Sigma 3$ GB emerging at the (111) surface with an adsorbed carbon atom at a Top 2 position. The groove area is located in the center of the sample. The high charge density is distributed uniformly on the surface.

In summary, using DFT calculations we demonstrate that C adsorption is more favored in the groove area compared to the non-defective clean surface, suggesting that grooves are attacked more severely by metal dusting phenomena and act as corrosion initiation and cementite seed formation centers, in agreement with the experimental finding of Chun *et al* [2].

3.2. Molecular dynamics results

The previous section presented C adsorption energies using DFT for a groove at one type of GB emerging at one specific surface. Further investigation using other types of GB would unfortunately requires working on larger GBs models that are out of reach with current computational capabilities at the DFT level. Hence, we now investigate the effect of a $\Sigma 5$ GB emerging on a (210) the surface using a reactive force field enabling us to tackle large sample sizes and reduce the finite size effects, and allowing us to perform a more detailed analysis of the CO molecule interaction with the defective surfaces.

More specifically, we perform a series of molecular dynamics (MD) simulations to evaluate the evolution of CO molecule dissociation rate as a function of: surface morphology, hydrogen content

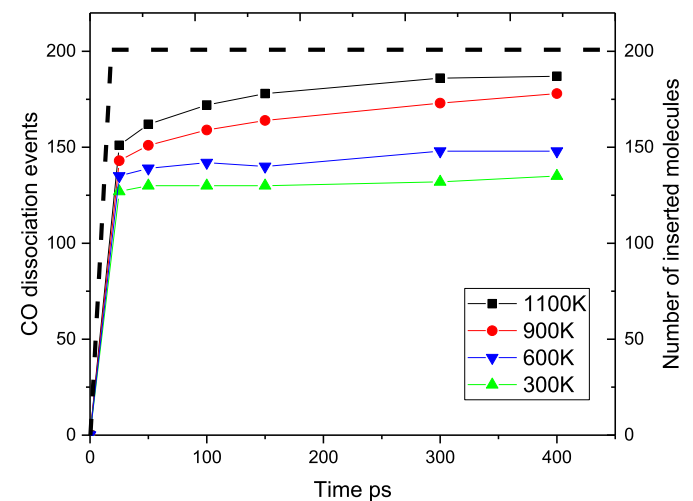


Fig. 5. Variation of CO dissociation events of a gas mixture 50%CO:50% H_2 molecules on a clean (111) surface as a function of time in ps at various temperatures for a total of 200 CO and H_2 molecules inserted.

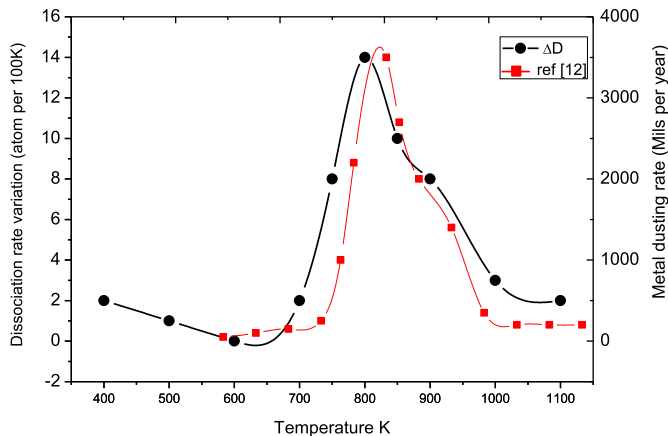


Fig. 6. (black circles) Dissociation rate variation as a function of temperature $\Delta D/\Delta T$ of a gas mixture 50%CO:50% H_2 molecules on a clean (111) surface. The results are taken after an MD simulation time of 120 ps. (red squares) experimental results by Chun et al. [2] for the temperature dependence of the metal dusting corrosion rate of the same gas mixture. (For interpretation of the references to colour in this figure legend, the reader is referred to the web version of this article.)

and temperature on both $\Sigma 3$ and $\Sigma 5$ grain boundaries emerging on the (111) and (210) surfaces and their corresponding ideal slabs with non-defective surfaces.

3.2.1. Temperature effect on CO dissociation on iron surfaces

To examine the effect of temperature, we calculate the CO dissociation rate at 300 K, 600 K, 900 K, and 1100 K by inserting simultaneously 200 CO and H_2 molecules at a rate of one molecule every 125 step. Fig. 5 presents the number of dissociated CO molecules as a function of time at various temperatures. The temperature dependent CO dissociation events feature two regimes: 1) a rapidly increasing dissociation rate as a function of time within the first 25 ps 2) a much slower dissociation dynamics stabilizing with time until reaching saturation. We associate the rapid dissociation regime from 0 to 25 ps to the progressive rise of the CO surface coverage with Fe and its high catalytic activity at the beginning of the CO molecules deposition. After 25 ps and once all the 200 CO

molecules are inserted, the surface coverage increases, hence lowering the catalytic activity of the Fe surface and the CO dissociation rate decreases considerably. Quantitatively, the dissociation events increase as a function of the simulated temperature indicative of a temperature dependent behavior as shown in Fig. 5. We estimate that the dissociation rate reached saturation when its variation as a function of time becomes negligible. For all the temperatures this is reached at 300 ps and will be used subsequently to generate Fig. 6.

Turning to the influence of temperature on the CO dissociation rate variation $\Delta D/\Delta T$, Fig. 6 shows the variation of the CO dissociation rate after saturation as a function of temperature. The dissociation rate variation increases drastically in the region starting from 650 K to 950 K with a peak around 800 K. This behavior compares well with the experimental results of temperature dependence of the metal dusting corrosion rate of iron in 50CO:50 H_2 gas mixture mentioned in C. M. Chun et al work [2]. Although there exists significant differences between their experiment and our simulation with respect to time and system scales, matching shape and peak location between the two results support a direct relation between the CO dissociation rate variation and the metal dusting corrosion as a function of temperature. Experimental data [2] are plotted along side with the curve obtained in our simulations in Fig. 6, showing that our MD simulation results are in good agreement with three of the four regimes mentioned in Ref. [2], namely: 1) a rapid rise of the metal dusting corrosion starting at 650 K, 2) the maximum is reached at 800 K, 3) a gradual decrease above 800 K. However, the first regime between 350 and 550 K mentioned in Ref. [2], that shows a gradual increase in corrosion rate with temperature with a very small slope, is not observed in here, probably because the dissociation rate is too small with respect to our simulation time.

3.2.2. The effect of grain boundary emerging at the surface on CO dissociation

In order to investigate the effect of a surface defect on the CO dissociation rate, we conducted a comparison between perfect and defective Fe surfaces containing an emerging GB with a V-shape groove at the center of the sample. To allow comparison, we investigate similar exposed areas as explained in the introduction. Fig. 7 shows a quantitative comparison between two GB types, a $\Sigma 3$

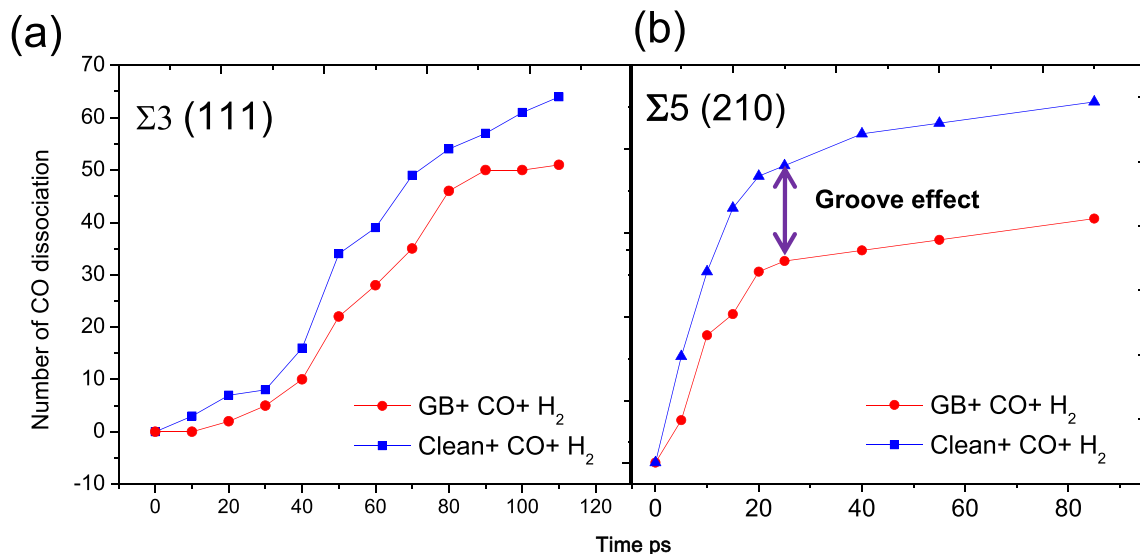


Fig. 7. Number of CO dissociations as a function of MD simulation time in the presence of a 50%CO+50% H_2 gas mixture for: (a) clean (111) surface as well as an emerging $\Sigma 3$ GB, and (b) a (210) clean surface as well as an emerging $\Sigma 5$ GB.

and a $\Sigma 5$ GB emerging at the (111) and the (210) surfaces respectively with a 50%CO:50%H₂ gas mixture and their corresponding clean surfaces. In both cases, we observe that the dissociation rate is higher on the defective surface, hence indicating a “groove effect”. Fig. 8 presents snapshots (produced by OVITO [24]), along the MD trajectory of CO dissociation on the $\Sigma 5$ GB and its corresponding (210) perfect surface. For a 50%CO:50%H₂ gas mixture reacting over bcc-Fe, we can visually see that the dissociation is higher in the groove area compared to the clean surface, especially at the step edges, confirming Fig. 7 results. Moreover, Fig. 8 shows the formation of new molecules such as CO₂ and H₂O generally after 20 ps of simulation time (more details in Fig. S1 of the supplementary materials). The relaxation of CO molecules on the surface and

dissociation leads to high oxygen concentration on the surface, while carbon atoms diffuse to the subsurface. The dissociation rate for the $\Sigma 5$ and $\Sigma 3$ emerging GBs is increased by 68% and 30% respectively, with respect to perfect surfaces. It should be noted that at the macroscopic level, the area occupied by this type of defect on the overall surface is generally smaller than the GB area in our model and can vary based on the material's microstructural morphology and grain size. This means that CO dissociation rate will change accordingly. Nevertheless, the high dissociation rate observed in the groove region is still indispensable for initiating corrosion and forming the first cementite seeds.

The dissociation rate of 100 CO molecules inserted on the two surfaces is found to be 4.0 atom/nm² for the (111) surface and 3.5

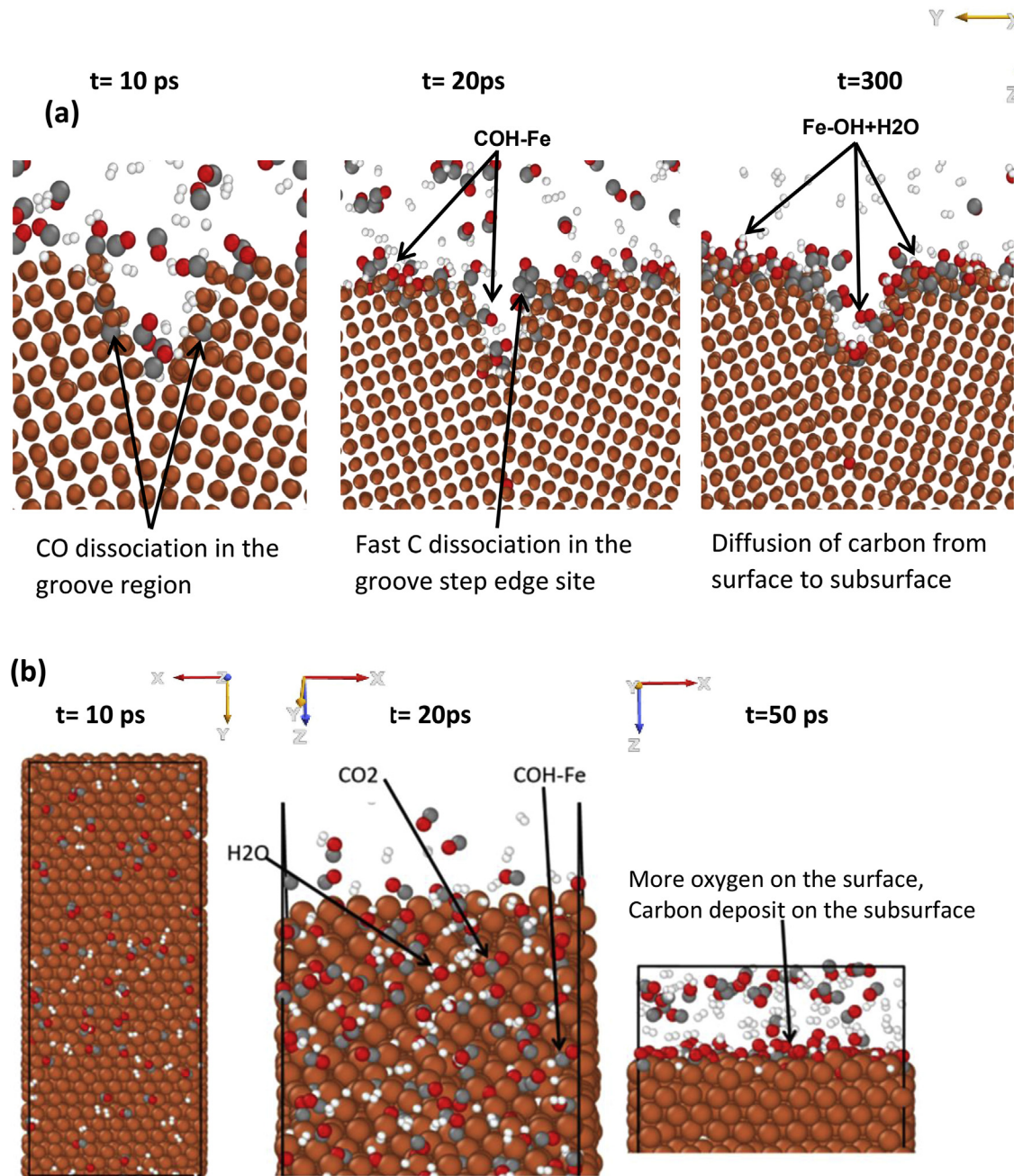


Fig. 8. Snapshots of the atomic configurations during ReaxFF MD simulations at 900 K for a 50%CO:50%H₂ gas mixture reacting over bcc-Fe with (a) a $\Sigma 5$ GB emerging at a (210) free surface and (b) a clean (210) surface.

atom/nm² for the (210) surface after 70 ps. These values indicate that the dissociation rate depends also on the cleaved surface. Section 3.1 in Ref. [25] shows that (110) and (210) are at the two ends of the spectrum of packing density, interlayer separation, and other related structural parameters; (111) lies somewhere in the middle. Moreover, the charge analysis in Table 5 of the same reference clearly indicates that the more packed the surface, the more electrons are available to the surface layers, which has a direct relation in reducing the dissociation barrier and thus increasing the dissociation rate. This result explains why the dissociation rate on a (111) surface is much higher than on a (210) surface (see Fig. 7). It should be noted that the dissociation rate depends also on the number of molecules inserted per MD step. This is observed, for the case of the $\Sigma 3$ GB, by comparing the evolution of the dissociation rate of Fig. 5 (200 molecules inserted in 25 ps) and that of Fig. 7 (100 molecules inserted in 100 ps). With the same methodology, the presence of hydrogen was found to enhance CO dissociation rate, its effect is discussed in details in the supplementary material. Statistics on CO dissociation and recombination rates on a (111) clean surface as a function of MD time in picoseconds with and without H₂ in the gas mixture confirm that H₂ enhances the CO dissociation rate. It helps to consume the resulting oxygen via the formation of water molecules, thus lowering the rate of the backward CO recombination reaction in favor of the formation of hydrocarbon molecules on the surface.

The effect of emerging GBs on enhancing CO dissociation rate and thus metal dusting is in agreement with experimental observations related to surface roughness. Grabke et al [26] published a thermogravimetric study of metal dusting in flowing CO + H₂ + H₂O gas atmosphere at 600 °C on samples with different microstructural iron grain sizes. They demonstrated that the grain size strongly affects metal dusting: very weak metal dusting corrosion was observed on the iron system with very fine grains after 150 h of experiment, whereas strong metal dusting corrosion was observed on coarse-grains system after only 30 h of experiment. Metal dusting is thus triggered by certain types of defects such as grain boundaries and cracks.

4. Conclusions

To better understand metal dusting corrosion in iron, the effect of grain boundaries emerging at free surfaces on carbon adsorption and CO dissociation was investigated. Density functional theory calculations demonstrate that C adsorption in the groove area is more favorable than on the clean surface. Molecular dynamics simulation of CO dissociation rate variation in the presence of hydrogen on a Fe (111) surface shows direct analogy with the experimental observation of metal dusting rate as a function of temperature. MD simulations comparing between clean and defective surfaces show that the groove area enhances CO dissociation rate and that the type of cleaved surface also has an effect. A comparison between a 50%CO:50%H₂ gas mixture, and CO gas only, shows that hydrogen greatly enhances CO dissociation on the iron surface. Hydrogen interacts with the dissociated oxygen atoms forming water, hence preventing CO recombination on the surface. It can also interact with carbon forming hydrocarbon on the Fe surface. Together these results provide a unified picture, from a microscopic point of view, on the role of surface defects, especially grain boundaries, in C adsorption leading to corrosion, a crucial aspect that had been largely ignored numerically until now. The present works offers a general understanding of the very early stages of the metal dusting corrosion initiation at very small time and length scales unveiling aspects hardly accessible experimentally. More work remains to be done to obtain a full atomic description of the kinetic processes associated with steel corrosion.

Future work will focus on other emerging grain boundaries, the effect of grain size on the CO dissociation as well as the effect of pressure on metal dusting speed, a phenomenon that has been well investigated experimentally but for which a detailed understanding is still lacking [27,28].

Acknowledgments

This work is supported by the Qatar National Research Fund (QNRF) through the National Priorities Research Program (NPRP 6-863-2-355). The advanced computing facility of Texas A&M at Qatar was used for all calculations. We would like to thank Dr Aurab Chakrabarty for helpful discussions.

Appendix A. Supplementary data

Supplementary data related to this article can be found at <http://dx.doi.org/10.1016/j.actamat.2017.06.049>.

References

- [1] A. Bałkowiec, J. Michalski, H. Matysiak, K. Kurzydłowski, Influence of grain boundaries misorientation angle on intergranular corrosion in 2024-T3 aluminium, *Mater. Sci.* 29 (2011) 305–311.
- [2] C.M. Chun, J.D. Mumford, T.A. Ramanarayanan, Mechanisms of metal dusting corrosion of iron, *J. Electrochem. Soc.* 149 (2002) B348–B355.
- [3] D.E. Jiang, E.A. Carter, Carbon atom adsorption on and diffusion into Fe (110) and Fe (100) from first principles, *Phys. Rev. B* 71 (2005) 45402.
- [4] T. Wang, X.-X. Tian, Y.-W. Li, J. Wang, M. Beller, H. Jiao, Coverage-dependent CO adsorption and dissociation mechanisms on iron surfaces from DFT computations, *ACS Catal.* 4 (2014) 1991–2005.
- [5] S. Booyens, M. Bowker, D.J. Willock, The adsorption and dissociation of CO on Fe (111), *Surf. Sci.* 625 (2014) 69–83.
- [6] A. Chakrabarty, O. Bouhali, N. Mousseau, C.S. Becquart, F. El-Mellouhi, Influence of surface vacancy defects on the carburisation of Fe 110 surface by carbon monoxide, *J. Chem. Phys.* 145 (2016) 44710.
- [7] O.A. Restrepo, N. Mousseau, F. El-Mellouhi, O. Bouhali, M. Trochet, C.S. Becquart, Diffusion properties of Fe–C systems studied by using kinetic activation–relaxation technique, *Comput. Mater. Sci.* 112 (2016) 96–106.
- [8] H.-S. Nam, D.J. Srolovitz, Molecular dynamics simulation of Ga penetration along $\Sigma 5$ symmetric tilt grain boundaries in an Al bicrystal, *Phys. Rev. B* 76 (2007) 184114.
- [9] T. Frolov, D.L. Olmsted, M. Asta, Y. Mishin, Structural phase transformations in metallic grain boundaries, *Nat. Commun.* 4 (2013) 1899.
- [10] D.E. Jiang, E.A. Carter, Diffusion of interstitial hydrogen into and through bcc Fe from first principles, *Phys. Rev. B* 70 (2004) 64102, <http://dx.doi.org/10.1103/PhysRevB.70.064102>.
- [11] C.-F. Huo, J. Ren, Y.-W. Li, J. Wang, H. Jiao, CO dissociation on clean and hydrogen precovered Fe (111) surfaces, *J. Catal.* 249 (2007) 174–184.
- [12] D. Jiang, E.A. Carter, Adsorption and diffusion energetics of hydrogen atoms on Fe(110) from first principles, *Surf. Sci.* 547 (2003) 85–98, <http://dx.doi.org/10.1016/j.susc.2003.10.007>.
- [13] M.M. Islam, C. Zou, A.C.T. van Duin, S. Raman, Interactions of hydrogen with the iron and iron carbide interfaces: a ReaxFF molecular dynamics study, *Phys. Chem. Chem. Phys.* 18 (2016) 761–771.
- [14] C. Zou, A. Van Duin, Investigation of complex iron surface catalytic chemistry using the ReaxFF reactive force field method, *JOM* 64 (2012) 1426–1437.
- [15] I.H. Sahputra, A. Chakrabarty, O. Restrepo, O. Bouhali, N. Mousseau, C.S. Becquart, F. El-Mellouhi, Carbon adsorption on and diffusion through the Fe (110) surface and in bulk: developing a new strategy for the use of empirical potentials in complex material set-ups, *Phys. Status Solidi (b)* 254 (2) (2017).
- [16] P.E. Blochl, Projector augmented-wave method, *Phys. Rev. B* 50 (1994) 17953.
- [17] G. Kresse, J. Furthmüller, Efficient iterative schemes for ab initio total-energy calculations using a plane-wave basis set, *Phys. Rev. B* 54 (1996) 11169.
- [18] J.P. Perdew, K. Burke, M. Ernzerhof, Generalized gradient approximation made simple, *Phys. Rev. Lett.* 77 (1996) 3865.
- [19] A. Chakrabarty, O. Bouhali, N. Mousseau, C.S. Becquart, F. El Mellouhi, Insights on Finite Size Effects in Ab-initio Study of CO Adsorption and Dissociation on Fe 110 Surface, 2016 arXiv Prepr. arXiv:1603.04662.
- [20] H.M. Aktulga, J.C. Fogarty, S.A. Pandit, A.Y. Grama, Parallel reactive molecular dynamics: numerical methods and algorithmic techniques, *Parallel Comput.* 38 (2012) 245–259.
- [21] K. Chenoweth, A.C.T. Van Duin, W.A. Goddard, ReaxFF reactive force field for molecular dynamics simulations of hydrocarbon oxidation, *J. Phys. Chem. A* 112 (2008) 1040–1053.
- [22] T.P. Senftle, S. Hong, M.M. Islam, S.B. Kylasa, Y. Zheng, Y.K. Shin, C. Junkermeier, R. Engel-Herbert, M.J. Janik, H.M. Aktulga, The ReaxFF reactive

- force-field: development, applications and future directions, *Npj Comput. Mater.* 2 (2016) 15011.
- [23] X. Sauvage, Y. Ivanisenko, The role of carbon segregation on nano-crystallisation of pearlitic steels processed by severe plastic deformation, *J. Mater. Sci.* 42 (2007) 1615–1621.
- [24] A. Stukowski, Visualization and analysis of atomistic simulation data with OVITO—the Open Visualization Tool, *Model. Simul. Mater. Sci. Eng.* 18 (2009) 15012.
- [25] P. Błoński, A. Kiejna, Structural, electronic, and magnetic properties of bcc iron surfaces, *Surf. Sci.* 601 (2007) 123–133.
- [26] H.J. Grabke, E.M. Muller-Lorenz, S. Strauss, E. Pippel, J. Woltersdorf, Effects of grain size, cold working, and surface finish on the metal-dusting resistance of steels, *Oxid. Met.* 50 (1998) 241–254.
- [27] H.J. Grabke, G. Tauber, H. Viefhaus, Equilibrium surface segregation of carbon on iron (100) faces, *Scr. Metall.* 9 (1975) 1181–1184.
- [28] T. Philomena, I.E. Minchington, C.W. Thomas, N. Briggs, A Study of the Relationship between Metal Dusting and Pressure, (n.d.).